

# Experimental and numerical study of oil drop motion within an ESP impeller

Rodolfo Marcilli Perissinotto<sup>1</sup> – rodolfoperissinotto@gmail.com

Mariana Gallassi<sup>2</sup> – mariana.gallassi@isdbflowtech.com

Gabriel F. N. Gonçalves<sup>2</sup> – gabriel.farah@isdbflowtech.com

William Monte Verde<sup>1</sup> – williammonteverde@gmail.com

Marcelo Souza de Castro<sup>1</sup> – mcastro@fem.unicamp.br

João Carneiro<sup>2</sup> – joao.carneiro@isdbflowtech.com

Jorge Luiz Biazussi<sup>1</sup> – biazussi@unicamp.br

Antonio Carlos Bannwart<sup>1</sup> – bannwart@fem.unicamp.br

<sup>1</sup>School of Mechanical Engineering, University of Campinas. Rua Mendeleev, 200, Cidade Universitária, Campinas-SP, CEP 13083-860.

<sup>2</sup>ISDB FlowTech. Rua Lauro Müller, 116/3006, Botafogo, Rio de Janeiro-RJ, CEP 22290-160.

## Abstract

The Electrical Submersible Pump (ESP) is a multistage centrifugal pump used in the petroleum industry as an artificial lift method. The ESP usually works with the presence of two-phase liquid-liquid flows that constitute dispersions and emulsions, causing performance losses and operational problems. This research aims to investigate the behavior and evaluate the dynamics of individual oil drops in an oil-in-water dispersion within an ESP impeller. The study adopts experimental and numerical approaches. Initially, experiments were performed using an experimental facility with a high-speed camera and an ESP prototype working at 600 rpm and 900 rpm, for water flows around the Best Efficiency Point (BEP) and with the injection of oil drops at a low flow rate. The acquired images were processed, and a drop sample was tracked, enabling the analysis of the size, shape, path, velocity, and acceleration of the oil drops. Numerical simulations were executed in ANSYS<sup>®</sup> software to define relevant parameters related to water and oil drops, such as velocities, accelerations, forces, turbulent dissipation, and residence time. The images reveal a unique flow pattern of dispersed drops in a continuous water phase. The oil drops' diameters vary from tenths of a millimeter to around 3 mm. The drops' trajectories can be classified into three different regions within the impeller channels. The drops' velocities stay in the order of 1 m/s, while accelerations can reach hundreds of m/s<sup>2</sup>. The velocity profiles show that the oil drops tend to decelerate during their trajectory, while the acceleration profiles suggest peaks at the channel inlet and outlet. High intense turbulence is present in the impeller entrance zone. The evaluation of the residence time and the particle Reynolds number suggest that smaller oil drops follow the water streamlines, while larger oil drops tend to be affected by external forces. The main forces that govern the oil drop motion are the drag, the pressure gradient, and the virtual mass forces. The force from the pressure gradient is tenfold greater than the force from the drag. The virtual mass effect is significant only in the impeller inlet. In general, in this research, numerical results show a satisfactory agreement with the experimental data.

**Keywords:** centrifugal pump, two-phase liquid-liquid flow, flow visualization, oil drop dynamics, CFD.

## Nomenclature

ESP	Electrical Submersible Pump	$f'(t)$	First derivative in finite-difference method
BEP	Best Efficiency Point	$f''(t)$	Second derivative in finite-difference method
HSC	High-Speed Camera	$\Delta t$	Time between two consecutive images
VSD	Variable Speed Driver	$h$	Time step in finite-difference method
PIV	Particle Image Velocimetry	$V_R$	Radial velocity of an oil drop
FBRM	Focused Beam Reflectance Measurement	$V_\theta$	Swirl velocity of an oil drop
CFD	Computational Fluid Dynamics	$\vec{V}$	Velocity of oil drop in non-inertial system
GVF	Gas Volume Fraction	$\vec{V}_I$	Velocity of oil drop in inertial system
VOF	Volume of Fluid	$A_R$	Radial acceleration of an oil drop
MRF	Moving Reference Frame	$A_\theta$	Swirl acceleration of an oil drop
DPM	Discrete Phase Model	$\vec{A}$	Acceleration of drop in non-inertial system
SMM	Sliding Mesh Model	$\vec{A}_I$	Acceleration of drop in inertial system
BSL	Reynolds Baseline Model	$\vec{F}_R$	Resultant force
RANS	Reynolds Averaged Navier-Stokes	$\vec{F}_D$	Drag force
SST	Menter's Shear Stress Transport	$\vec{F}_P$	Pressure gradient force
FG	Full Geometry	$\vec{F}_L$	Lift force
RG	Reduced Geometry	$\vec{F}_{VM}$	Virtual mass force
VM	Virtual Mass	$m_p$	Oil drop mass
$g$	Gravity	$d$	Oil drop diameter
$N$	Rotational speed of impeller	$\nabla_s p$	Pressure gradient
$\omega$	Angular speed of impeller	$d_{ij}$	Deformation tensor
$D$	Impeller diameter	$C_D$	Drag coefficient
$N_c$	Number of impeller channels	$C_{VM}$	Virtual mass effect
$m_w$	Water mass flow rate	$K$	Constant in Saffman's lift force equation
$Q$	Water volume flow rate	$A$	Constant in normalized oil drop position
$Q_{BEP}$	Water flow rate at BEP	$p$	Static pressure
$q$	Fraction of $Q_{BEP}$	$P$	Modified pressure
$T$	Temperature of water	$\vec{U}$	Velocity of water
$P_1$	Pressure at the inlet of ESP prototype	$\rho$	Water density
$P_2$	Pressure at the outlet of ESP prototype	$\mu$	Water viscosity
$\Delta P$	Difference between pressures $P_1$ and $P_2$	$\mu_t$	Turbulent viscosity
$\rho_o$	Oil density	$\mu_{ef}$	Effective viscosity
$\mu_o$	Oil viscosity	$\Phi$	Dimensionless flow rate
$\sigma_{a/o}$	Oil-air surface tension	$\Psi$	Dimensionless pump head
$\sigma_{w/o}$	Oil-water interfacial tension	$\kappa$	Turbulent kinetic energy
$x, y$	Oil drop position in Cartesian reference	$\epsilon$	Turbulent eddy dissipation
$R, \theta$	Oil drop position in polar reference	$t_{res}$	Impeller residence time
$z$	Position perpendicular to $xy$ or $R\theta$ planes	$t_{res}^*$	Normalized residence time
$R^*, \theta^*$	Normalized oil drop position	$Re_d$	Particle Reynolds number
$R_i, R_o$	Impeller radius: from center to inlet and outlet	$U_{tip}$	Blade velocity
$\theta_0$	Initial angle of an oil drop	$y^+$	Dimensionless distance from the wall
$\theta_c$	Channel angle	$f^+(R^*)$	Central path position function
$\dot{R}, \dot{\theta}$	First derivatives of drop position	$f^-(R^*)$	Central path position function
$\ddot{R}, \ddot{\theta}$	Second derivatives of drop position		

## 1. Introduction

The petroleum industry uses the term lifting to refer to the process of vertically transporting fluids extracted from a reservoir, which must flow from the bottom of the well to the production facilities. When the reservoir pressure is insufficiently high to overcome the weight of the fluid column as well as the frictional pressure drop, producers must rely on external energy provided by artificial lifting methods.

One of the most consolidated techniques for lifting oil is the electrical submersible pumping, in which the fluids are elevated by a multiple-stage centrifugal pump, called Electrical Submersible Pump (ESP). ESPs are largely used in onshore and offshore wells, with low and high liquid flow rates (Takacs, 2017). It is estimated that around the world more than 100,000 wells operate with ESPs (Flatern, 2015).

Although ESPs are widely employed, several aspects related to their usage are still problematic. This is especially the case when it comes to operating in the presence of gas or viscous fluids, conditions quite common in applications associated with the petroleum industry. Examples of operation with high-viscosity fluids include heavy oil fields and the formation of liquid-liquid mixtures when water is present. In this last case, the phase distribution can be arranged as a dispersion, depending on the flow conditions.

Indeed, oil production is closely related to the occurrence of dispersions and emulsions (Abivin *et al.*, 2009). Their formation depends on mechanical processes that provide the energy necessary to dissipate one liquid into the other (Sjoblom, 2005). In this sense, the ESP can promote the creation of dispersions, due to the fluids being agitated in the impeller, resulting in the break-up of phases into small droplets.

The apparent viscosity of a dispersion may be higher than the pure oil viscosity. In the case of ESPs, the presence of water can increase the effective petroleum viscosity and consequently impair pump performance, leading to a significant rise in operational costs. The behavior of real flows is very different from that observed in single-phase flows. Thus, the project of designing an ESP system calls for engineers to possess a detailed comprehension of multiphase flow dynamics within centrifugal pumps.

Considerable efforts have been made to investigate two-phase flows inside pumps. Computational Fluid Dynamics (CFD) methods are commonly adopted to simulate flow in a computational environment and may provide detailed insight into flow fields and dynamics. Flow-visualization techniques are used to experimentally identify flow patterns and analyze the interaction between the phases present in a mixture. A powerful method for flow visualization is the high-speed imaging, as it helps researchers to observe transient phenomena with a satisfactory spatial and temporal resolution (Mohammadi and Sharp, 2013).

Regarding two-phase gas-liquid flows, initial studies were focused on the nuclear industry, where centrifugal pumps were employed in reactor cooling systems and there was a concern about radioactive fluids leaking. The pioneer in the petroleum industry was Estevam (2002), who developed the first ESP prototype for experimental visualization of air-water flows.

Two-phase gas-liquid flows within pumps were also examined by such authors as Barrios and Prado (2011), Trevisan and Prado (2011), Zhang *et al.* (2016), Monte Verde *et al.* (2017), and Cubas Cubas (2017). These authors, who used high-speed cameras to visualize flow in impellers, aimed to identify flow patterns; observe the phenomena as accumulation, agglomeration, and coalescence; and investigate how the behavior of bubbles was influenced by rotation speed, liquid flow rate, intake pressure, viscosity, and surface tension.

Caridad and Kenyery (2004), Caridad *et al.* (2008), Barrios *et al.* (2009) and Pineda *et al.* (2016) studied gas-liquid flows inside ESPs using CFD simulations. Caridad and Kenyery (2004) adopted a two-fluid model to predict pressure, velocity fields, and Gas Volume Fraction (GVF). To model turbulence, the authors used the  $\kappa$ - $\epsilon$  model. They successfully predicted the presence of gas pockets for different GVFs inside the pump. Later, Caridad *et al.* (2008) investigated the ESP head, bubble diameter, flow angle at the impeller outlet and phase distribution within the channels. The results presented excellent agreement with experimental data. The authors predicted that, due to the low velocity of the liquid, the gas would agglomerate on the high-pressure side of the

impeller blade. The  $\kappa$ - $\epsilon$  turbulence model was also used by Barrios *et al.* (2009) to perform one-fluid and two-fluid simulations. They observed some vortices at the trailing edge on the suction side and also noticed a recirculation zone inside the channels. Using a correlation for the drag coefficient, the authors verified an accumulation of gas at the intake. Finally, Pineda *et al.* (2016) used the Volume of Fluid (VOF) model to obtain the void fraction and the pump head. In a comparison with experimental measurements, the CFD was capable, under certain conditions, of determining the flow behavior. Fluctuations occurred only at high rotation speeds.

Minemura and Murakami (1980), Sabino (2015) and Ofuchi *et al.* (2017) explored the air bubble dynamics inside impeller channels. According to them, the movement of the bubbles in the pump is controlled by five forces: a drag force due to the movement of the bubble relative to the water, a pressure force related to the pressure gradient in the channel, a buoyancy force due to the difference of densities between the fluids, an inertial force as a consequence of the water acceleration and a force that considers the historical effect of the flow around the bubble. However, the authors agree that, in the cases investigated, the most important forces acting on air bubbles were the drag force and the pressure gradient force.

Concerning two-phase liquid-liquid flows, pipelines are dealt with in the vast majority of works, such as those by Brauner and Maron (1992), Alkaya *et al.* (2000), Angeli and Hewitt (2000), Lum *et al.* (2006), Rodriguez and Oliemans (2006), Vielma *et al.* (2007), Grassi *et al.* (2008), Wang *et al.* (2011), Castro *et al.* (2012), Rodriguez and Baldani (2012), Hanafizadeh *et al.* (2015), Loh and Premanadhan (2016) and Cavicchio *et al.* (2018). In the scope of centrifugal pumps, experimental studies on dispersions and emulsions are few, such as Khalil *et al.* (2008), Morales *et al.* (2013) and Bulgarelli *et al.* (2017a, 2017b). There are also some numerical works related to ESPs, including those by Mundo (2014), Stel *et al.* (2015) and Zhu *et al.* (2016), the last ones concerning multistage pumps. However, no studies are available that focus on dynamics of individual liquid droplets.

Khalil *et al.* (2008) experimentally investigated the performance of centrifugal pumps working with oil-in-water emulsions. The authors concluded that the presence of emulsions degrades the pump head and efficiency. The performance also suffers a reduction when the holdup and temperature decrease.

Morales *et al.* (2013) studied the dispersion formation in a pump working with a dispersion of water and oil. The authors used a particle-size analyzer to measure the drop-size distribution and concluded that the drop size mostly depends on the pump rotation. The drops become smaller as the rotation increases.

Mundo (2014) conducted experimental and numerical evaluations for water-in-oil emulsions within an ESP. The author studied the effect of water fraction and drop size on performance curves, using a BSL turbulence model (Reynolds Baseline Model). For both oils tested, the author verified that there was a reduction in the head and flow rate capacity and an increase of the emulsion effective viscosity with higher concentration.

Stel *et al.* (2015) performed CFD simulations in order to investigate the single-phase flow in a multistage ESP. They evaluated the influence of the turbulence model and the number of stages on the pump performance and compared some numerical and experimental results. The authors verified that the SST turbulence model (Menter's Shear Stress Transport) was more suitable for their system.

Zhu *et al.* (2016) were interested in the oil-viscosity effect on multistage ESPs. They conducted experimental analysis and numerical simulations, varying oil viscosity, flow rate and rotation speed. Steady-state simulations with SST turbulence model indicated that the pump efficiency starts to decrease when the oil viscosity is higher than 200 cP.

Bulgarelli *et al.* (2017a, 2017b) used an 8-stage ESP operating with emulsions to study the phase inversion phenomena and the chord-length distribution. Tests were carried out at various viscosities and rotation speeds. The phase inversion occurs at water fractions ranging between 10% and 30%. For low water fractions, oil is the continuous phase, with a higher effective viscosity that degrades the pump performance. For high water fractions, water is the continuous phase, with a lower effective viscosity that increases the pump performance.

Using a Focused Beam Reflectance Measurement (FBRM) technique, the authors observed that the chord length increased up to the phase inversion point and dropped after it.

In short, as the literature review exposes, the two-phase liquid-liquid flows with dispersions in ESPs are still insufficiently understood, despite their relevant application in the petroleum industry. Unlike their study of gas bubbles, researchers have not thoroughly investigated liquid droplets. Most studies in the literature examine the overall pump performance, but there is a lack of studies exploring the dynamics of liquid phases.

The objective of this research is to study, through a joint study of experiments and numerical simulations, the motion and the dynamics of individual liquid drops subject to a rotating field. First, oil drops are visualized in a turbulent water flow inside the impeller of an ESP prototype. Images are captured and processed to obtain size, shape, position, trajectory, velocity and acceleration of oil drops. The flow is then simulated using a CFD method, permitting the evaluation of turbulent dissipation, residence time, velocities, accelerations and forces. Finally, numerical results are compared with the experimental ones.

The results can provide a better understanding of the motion of dispersed droplets in pumps. This paper contributes to a better understanding of dispersions in two-phase flows within ESPs. In the future, the results can be expanded to other cases and associated with the efficiency and performance of different pumps. In addition, the slip between the phases can be calculated when water and oil velocities are evaluated. The long-term industrial application is the proposition of one-dimensional models in order to predict the best type of ESP for each application, but also to find optimum operational parameters for a given system.

## 2. Experimental Methodology

An experimental facility with an ESP prototype was used to perform experiments at different operational conditions. Water and a mineral oil were selected to compose the two-phase liquid-liquid flow. A High-Speed Camera (HSC) was employed to capture images of the flow within the prototype impeller.

### 2.1 Experimental Facility

The tests were performed using an experimental setup that consists of a water circuit, an oil injection system, and a visualization prototype based on the Baker-Hughes ESP P23. The ESP prototype was designed and built by Monte Verde *et al.* (2017), who minutely present the pump characteristics and the impeller geometry. The test bench is shown in **Fig. 1**.



**Fig. 1.** Photograph of the experimental facility with the visualization prototype.

The ESP prototype has an impeller with a transparent top shroud made of an acrylic material, which enables the visual access to the flow in all the channels. Monte Verde *et al.* (2017) used the prototype to study gas-liquid two-phase flows. In this current work, the test bench was updated to enable the visualization of liquid-liquid two-phase flows as well.

A high-speed camera model VEO 640, manufactured by Phantom<sup>®</sup>, is responsible for the flow visualization. The equipment acquires images with a maximum resolution of 2560 x 1600 pixel at a rate of 1400 frames per second. Three LED reflectors are used as light sources, each with 84 Watts and 7700 lumens.

A schematic illustration of the experimental facility is presented in **Fig. 2**. In the water line, a booster pump draws the liquid from a 0.5 m<sup>3</sup> separation tank. The water flows through a Coriolis meter and a shell-and-tube heat exchanger, before finally reaching the prototype suction. At the same time, in the oil line, a peristaltic pump draws the liquid out of a 10-liters reservoir. The oil is injected into the prototype near the impeller inlet through a capillary tube with 1/16-inch inner diameter. The oil becomes dispersed in the water flow. Both liquids enter, traverse and exit the impeller channels, while the high-speed camera captures images of the flow. The dispersion then goes to the separation tank where, by differences in density, the water is gravitationally separated from the oil. The water flows back to its line, while the separated oil is dewatered and returns to the oil tank.

The Coriolis flowmeter model RHM12, fabricated by Metroval, measures the water mass flow rate ( $m_w$ ). It has a limit range of 6000 kg/h and an accuracy of 0.2%. A resistance temperature detector type PT100, manufactured by ECIL, with 1/10 DIN accuracy, quantifies the dispersion temperature ( $T$ ) in the prototype inlet. Two capacitive pressure transducers series 2088, manufactured by Emerson Rosemount<sup>™</sup>, measure the intake ( $P_1$ ) and discharge ( $P_2$ ) pressures with an accuracy of 0.05%. The analog output signals are acquired by a National Instruments system. The data is monitored, processed and stored in a computer by a LabVIEW<sup>®</sup> code. In addition, the prototype rotation speed ( $N$ ) is checked manually with a digital tachometer model MDT-2238A, fabricated by Minipa, with an accuracy of 0.05%.

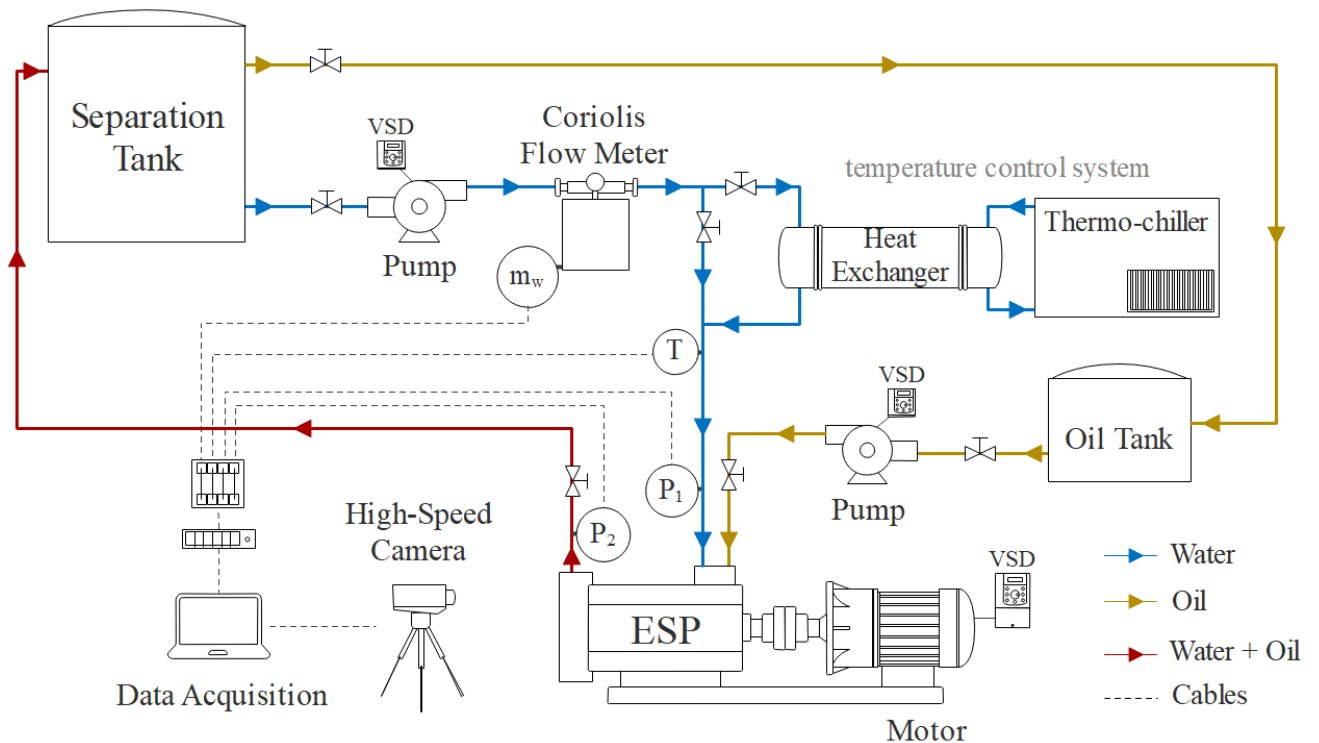


**Fig. 2.** Schematic diagram of the experimental facility.

As the fluids are flowing in a closed loop, they tend to heat up during the experiments. The temperature-control system, composed of the heat exchanger and a thermo-chiller, is able to maintain the fluids at a constant temperature. The system can also heat or cool the liquids; it is thus possible to modify their properties during the tests, especially the viscosity.

Control valves regulate pressure levels and flow rates in the lines. Moreover, each pump is controlled by a Variable Speed Driver (VSD) that sets the rotational speed and thus changes the flow rate. The rotational speed of the peristaltic pump is used to quantify the oil flow rate, which has very low values when compared to the water flow rate.

## 2.2 Test Matrix

Performance curves were determined for the ESP prototype operating with a water single-phase flow and an oil-water two-phase flow. The results were used as a reference for the visualization experiments.

The visualization tests for oil-in-water dispersions were carried out at two rotation speeds ( $N$ ) and three water volume flow rates ( $Q$ ) around the best efficiency points (BEP), as presented in **Table 1**. In all the tested conditions, the oil was injected at a constant flow rate of 2 ml/s, i.e., 0.007 m<sup>3</sup>/h.

**Table 1.** Test matrix with six flow conditions.

$N$ [rpm]	0.8 $Q_{BEP}$ [m <sup>3</sup> /h]	1.0 $Q_{BEP}$ [m <sup>3</sup> /h]	1.2 $Q_{BEP}$ [m <sup>3</sup> /h]
600	1.70	2.13	2.56
900	2.56	3.20	3.84

The water flow rates corresponding to the best efficiency points ( $Q_{BEP}$ ) were determined by the analysis of the single-phase performance curves.

As already mentioned, the two-phase liquid-liquid flow is a mixture of tap water and a mineral oil. Chemical tests were executed to characterize the oil properties at 25 °C; the tests yielded a density ( $\rho_o$ ) of 880 kg/m<sup>3</sup>, a dynamic viscosity ( $\mu_o$ ) of 220 cP, a surface tension ( $\sigma_{a/o}$ ) of 32 mN/m, and an interfacial tension ( $\sigma_{w/o}$ ) of 34 mN/m. All performance and visualization experiments were carried out at the temperature of 25 °C.

The originally transparent oil was darkened with a black dye to enhance the contrast between the liquid and the white impeller. A higher contrast improves the quality of the flow images. The dye does not affect the oil chemical properties nor the water color.

Even though the rotation speeds employed in real ESPs in the petroleum industry can reach 3500 rpm, some restrictions in the experiments limited the chosen test conditions to 600 rpm and 900 rpm. At high rotational speeds and flow rates, the oil drops become so small that the high-speed camera resolution is not sufficient to capture adequate images. Moreover, the ESP acrylic shroud may suffer severe damages and may even break when subjected to high pressures.

## 2.3 Experimental Procedure

In the performance tests for a single-phase flow, the prototype rotation remains constant throughout the test. The water flow rate is first adjusted to a maximum value that coincides with a zero-pressure generated by the ESP prototype. This condition is called open-flow. Afterward, data is acquired at 1 kHz frequency during 30 seconds and the average quantity is storage. Next, the discharge control valve is slightly closed to reduce the water flow rate and data is acquired again. In this condition, the flow rate is below the maximum and the pump head is above zero. The procedure is repeated until the water flow rate reaches a minimum value that correlates with the ESP highest-pressure, a condition called shut-off. Then, the prototype rotation is updated and the test is carried out from the beginning.



The procedure adopted for the two-phase flow performance tests is similar to the previous one. The only difference is the injection of oil at a constant flow rate. As the water flow decreases, the oil fraction increases.

However, the visualization experiments for two-phase oil-in-water flow have a quite different procedure. Before the test, the position of the LED reflectors is carefully adjusted to avoid forming shadows, the camera is placed on a tripod and the lens is focused on the impeller. The desired ESP rotation is set and remains constant throughout the test. Initially, the water pump and the discharge control valve are operated to obtain the desired water flow rate. In the oil injection system, the control valves are opened and the peristaltic pump is turned on. Next, the high-speed camera captures flow images for 10 seconds. While the images are saved in the computer hard disk, the peristaltic pump is turned off and the oil control valves are closed. After a few minutes, when the storage is complete, a new condition is established in the water loop. Then, the oil injection and the image acquisition restart. The procedure is repeated for all water flow rates. Finally, the test is performed again, at a different prototype rotation speed.

### 3. Image Analysis

The visualization tests for liquid-liquid two-phase flow resulted in thousands of images. An observation of them indicates the occurrence of a flow pattern characterized by dispersed oil drops in a water flow. The image processing reveals the characteristics of the oil drops, as well as allows the analysis of their dynamics, with an evaluation of velocities, accelerations, and forces.

#### 3.1 Image Observation

The flow images confirm the presence of dispersions within the impeller. The dispersed oil drops in water occur at all operational points considered in the test matrix, constituting a unique flow pattern. In addition, most drops have a spherical geometric shape, with only a few presenting irregular formats. The oil drops have equivalent diameters of tenths of a millimeter to about 3 mm. Furthermore, the drop size directly depends on the ESP rotation and the water flow, as shown in **Fig. 3**, **Fig. 4**, and **Fig. 5**, which compare the impeller under different tested conditions.

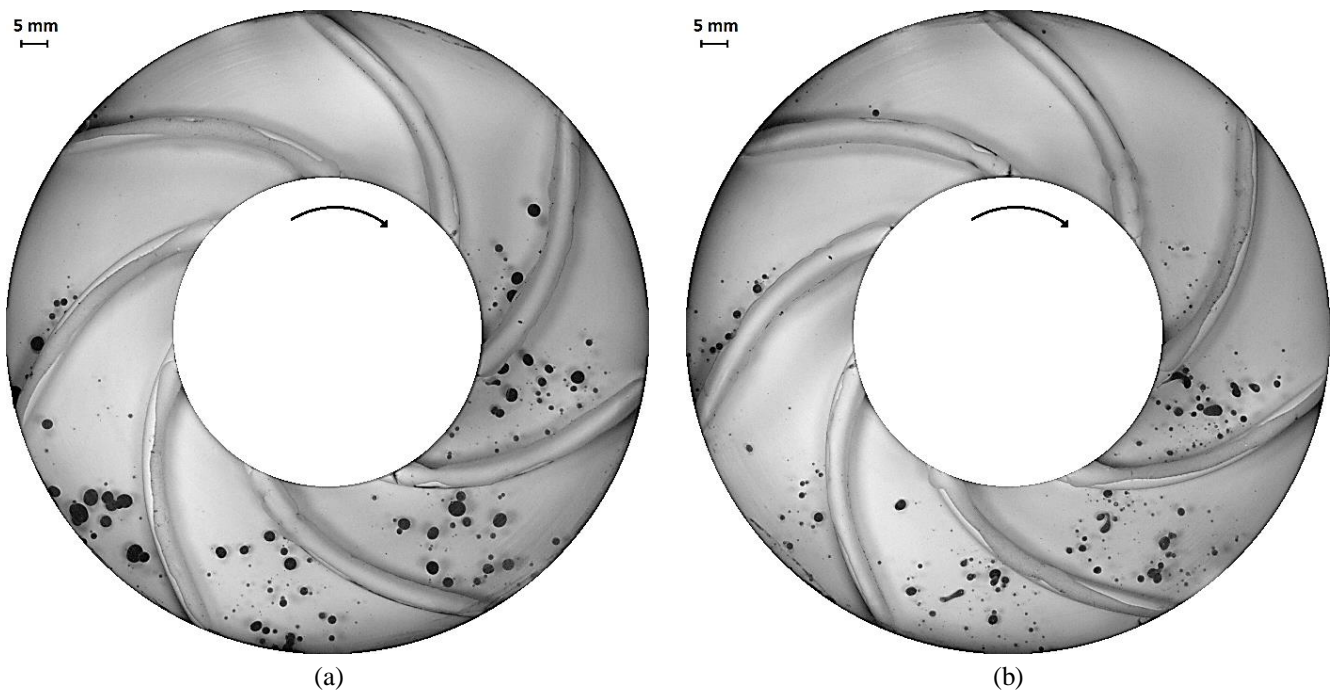


**Fig. 3.** Oil drops in the impeller at  $Q_{BEP}$ : (a) 600 rpm and (b) 900 rpm.



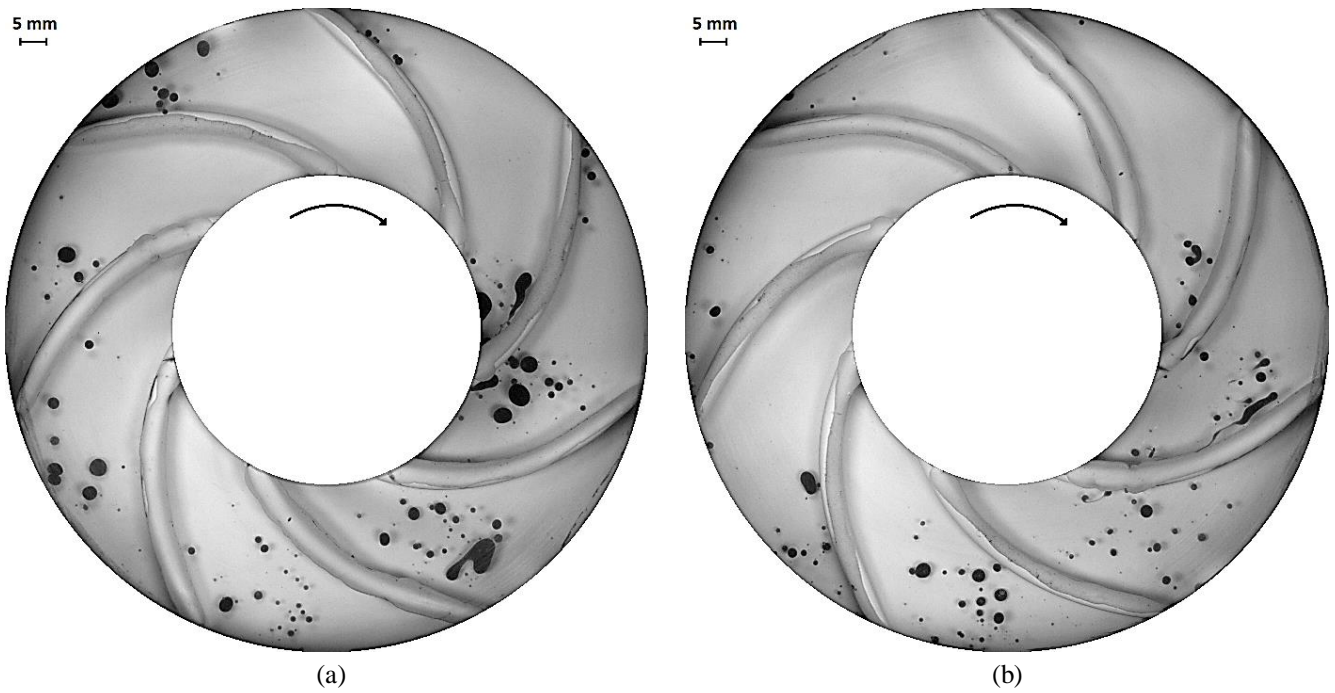


**Fig. 4.** Oil drops in the impeller at 600 rpm: (a)  $0.8 Q_{BEP}$  and (b)  $1.2 Q_{BEP}$ .

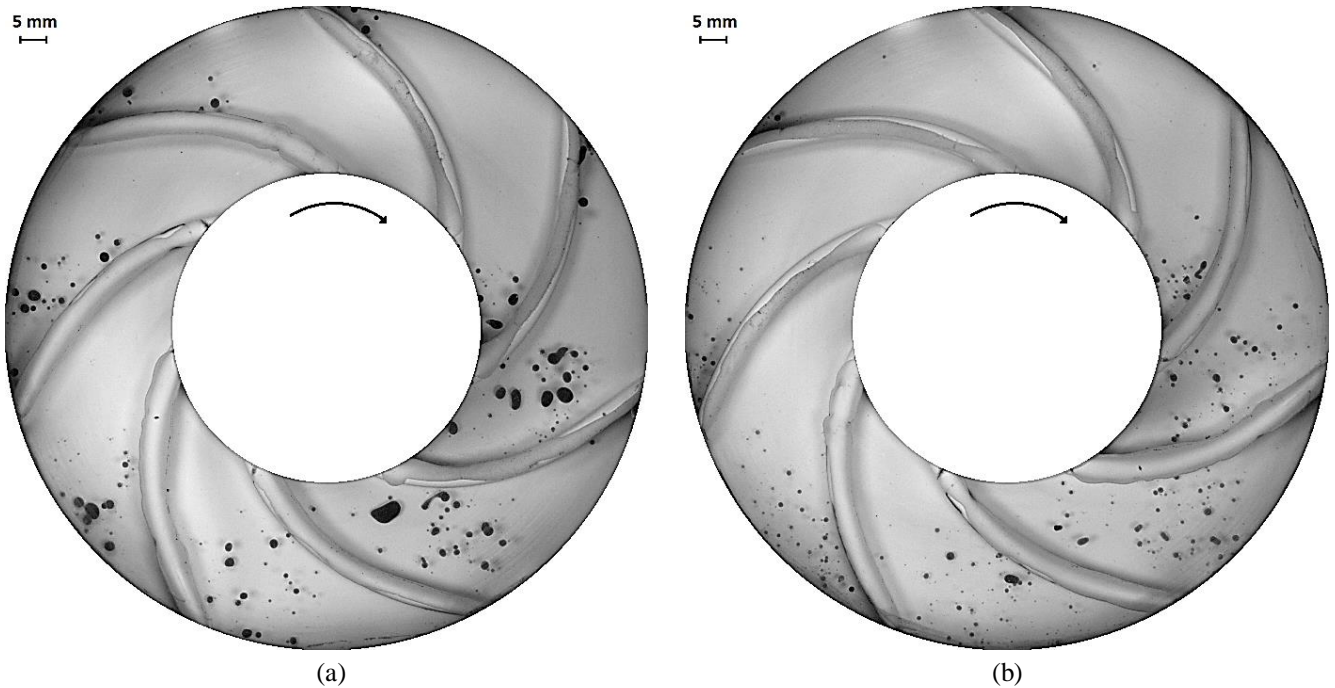


**Fig. 5.** Oil drops in the impeller at 900 rpm: (a)  $0.8 Q_{BEP}$  and (b)  $1.2 Q_{BEP}$ .

Clearly, the oil drop size varies as a function of the flow characteristics. The drops become smaller as pump rotation and water flow rate increase. The phenomenon is a consequence of higher local stresses, turbulence, and centrifugal field acting on the oil drops. Breakage and coalescence are virtually not observed in the image analysis. In fact, the oil drops tend to break before the impeller inlet, on the way from the injection point to the channel inlet where flow restrictions cause a high localized shear and the dispersion suffers a sudden change of direction.

### 3.2 Image Processing

The images were processed in a computational environment in order to enable the analysis of the oil drop trajectory and the evaluation of its dynamics. A MATLAB<sup>®</sup> routine rotated each image counterclockwise. As a result, the channels became static, as if the high-speed camera rotated integrally with the impeller during the experiments. The reverse rotation technique facilitates the analysis of the oil drops inside each channel without the impeller angular motion.

Then, using the software IDT Motion Studio, samples of oil drops were tracked from the images of the ESP prototype operating at the test matrix conditions, described in **Table 1**. The selected oil drops have diameters approximately from 1.0 mm to 2.5 mm. They execute well-behaved trajectories within the channels.

The tracking process creates a table with the oil drop position as a function of time, in a Cartesian coordinate system. The position,  $x$  and  $y$ , is converted to a new position,  $R$  and  $\theta$ , in the directions  $\hat{i}_R$  and  $\hat{i}_\theta$ , in polar coordinates with origin in the center of the impeller, as **Fig. 6** illustrates. The frame of reference is non-inertial since it rotates along with the impeller, due to the reverse rotation technique.

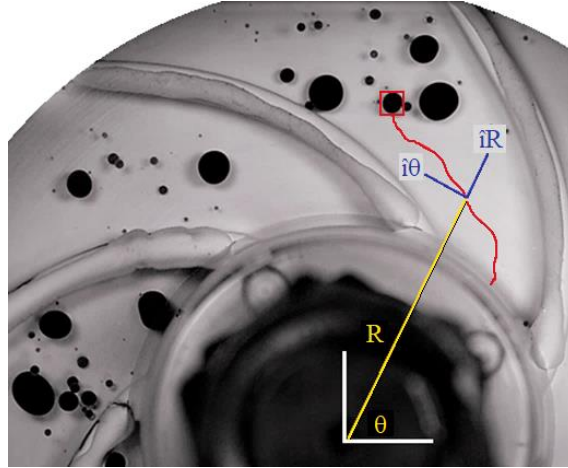


**Fig. 6.** Position of oil drop in a polar coordinate system.

The  $R$  and  $\theta$  values are used to calculate the radial and swirl velocities,  $V_R$  and  $V_\theta$ , and the radial and swirl accelerations,  $A_R$  and  $A_\theta$ . In a Lagrangian approach, they are obtained through the derivatives and the chain rule. As Hibbeler (2010) explained, considering the oil drops as rigid particles of negligible size, the velocity and acceleration are determined as:

$$\vec{V} = V_R \hat{i}_R + V_\theta \hat{i}_\theta = \dot{R} \hat{i}_R + R\dot{\theta} \hat{i}_\theta \quad [3.1]$$

$$\vec{A} = A_R \hat{i}_R + A_\theta \hat{i}_\theta = (\ddot{R} - R\dot{\theta}^2) \hat{i}_R + (R\ddot{\theta} + 2\dot{R}\dot{\theta}) \hat{i}_\theta \quad [3.2]$$

The particle velocity,  $V$ , and acceleration,  $A$ , are then converted from the rotating non-inertial frame of reference to a new fixed inertial one, with origin still in the impeller center. According to White (2011), the procedure consists of including effects such as the tangential velocity due to the rotation,  $\omega \times R$ , and the centrifugal and Coriolis pseudo-accelerations,  $\omega \times (\omega \times R)$  and  $2\omega \times V$ . Thus, the inertial velocity and acceleration,  $V_I$  and  $A_I$ , are evaluated as:

$$\vec{V}_I = \dot{R} \hat{i}_R + (R\dot{\theta} - \omega R) \hat{i}_\theta \quad [3.3]$$

$$\vec{A}_I = [\ddot{R} - (\omega + \dot{\theta})^2 R] \hat{i}_R + [R\ddot{\theta} + 2(\omega + \dot{\theta})\dot{R}] \hat{i}_\theta \quad [3.4]$$

The number of dots on  $R$  and  $\theta$  represent their first and second derivatives in time, i.e.,  $dR/dt$ ,  $d\theta/dt$ ,  $d^2R/dt^2$  and  $d^2\theta/dt^2$ . Since the oil drop position is given in the form of a matrix, the derivatives should be calculated via numerical derivation. Hence, the derivatives are obtained by the central finite-difference method, with a step  $h = \Delta t$ , the time interval between two consecutive images captured by the camera during the experiments. The finite-difference method is described by the equations below, where  $f'(t)$  and  $f''(t)$  are the derivatives of a generic function  $f(t)$ . In this paper, the function  $f(t)$  represents  $R$  and  $\theta$ :

$$f'(t) \approx \frac{f(t+h) - f(t-h)}{2h} \quad [3.5]$$

$$f''(t) \approx \frac{f(t+h) - 2f(t) + f(t-h)}{h^2} \quad [3.6]$$

With the velocities and accelerations, a resultant force can be calculated. The next section describes the mathematical modeling of the main forces acting on oil drops in the oil-in-water dispersions.

#### 4. Drop Motion

The oil drop dynamics is investigated using a force balance on the drop. The resultant force  $\vec{F}_R$  governs the motion of an oil drop with a mass  $m_p$  and is considered here as a sum of drag force ( $\vec{F}_D$ ), pressure force ( $\vec{F}_P$ ), lift force ( $\vec{F}_L$ ), and virtual mass force ( $\vec{F}_{VM}$ ). From Newton's second law:

$$\vec{F}_R = m_p \frac{d\vec{V}}{dt} = \vec{F}_D + \vec{F}_P + \vec{F}_L + \vec{F}_{VM} \quad [4.1]$$

Considering an oil drop with a spherical shape, the mass is estimated as a function of the oil density,  $\rho_o$ , and the drop diameter,  $d$ . Hence, the resultant force is obtained by:

$$\vec{F}_R = \rho_o \left( \frac{\pi d^3}{6} \right) \vec{A} \quad [4.2]$$

Regarding a spherical oil drop, the drag force is described as follows:

$$\vec{F}_D = \frac{1}{2} \rho C_D \left( \frac{\pi d^2}{4} \right) (\vec{U} - \vec{V}) |\vec{U} - \vec{V}| \quad [4.3]$$

where  $\rho$  is the water density,  $C_D$  is the drag coefficient,  $d$  is the oil drop diameter,  $\vec{U}$  and  $\vec{V}$  are respectively the water and oil drop velocities that determine the relative speed between continuous and dispersed phases. There are many correlations to calculate the drag coefficient in the literature. The drag coefficient model applied in this work is the Spherical Drag Law (Morsi and Alexander, 1972).

For a spherical oil drop, the force due to the pressure gradient is defined as follows:

$$\vec{F}_P = \frac{\pi d^3}{6} \nabla_s p \quad [4.4]$$

where  $\nabla_s p$  is the pressure gradient along the oil drop path.

The Saffman's lift force is calculated as follows:

$$\vec{F}_L = \frac{\pi d^2}{6} \frac{2K\nu^{0.5}\rho d_{ij}}{(d_{lk}d_{kl})^{0.25}} (\vec{U} - \vec{V}) \quad [4.5]$$

where  $K = 2.594$  and  $d_{ij}$  is the deformation tensor.

This expression for the lift force is valid for small particle sizes, normally smaller than one  $\mu\text{m}$ , with the particle Reynolds number much lower than the unit. In the present work, the lift force is disregarded, since the oil drop diameters are in the range from 0.01 mm to 10 mm.

Finally, the virtual mass force, generated by the acceleration of the fluid near the oil drop, is:

$$\vec{F}_{VM} = \frac{\pi d^3}{6} C_{VM} \rho \left( \vec{V} \cdot \nabla \vec{U} - \frac{d\vec{V}}{dt} \right) \quad [4.6]$$

where  $C_{VM} = 0.5$  is the virtual mass coefficient for spherical drops.

In the case of gas-liquid systems, Minemura and Murakami (1980) and Crowe *et al.* (1998) state that drag and pressure forces are the most relevant to the dispersed phase motion. This may be attributed to the low-density ratio between dispersed and continuous fluids. However, the same is not necessarily true for liquid-liquid systems, and the other forces may not be neglected at first.

Unfortunately, it is not possible to calculate the values of  $\vec{F}_D$ ,  $\vec{F}_P$ ,  $\vec{F}_L$  and  $\vec{F}_{VM}$  directly from the experiments, because of the water velocity,  $\vec{U}$ , and the pressure gradient,  $\nabla_s p$ , are both unknown. Thus, a CFD numerical simulation is an interesting tool to further investigate the oil dynamics. In a future experimental approach, it would be a good choice to use Particle Image Velocimetry (PIV), with the purpose of studying the water flow.

CFD simulations can assess the velocities, accelerations, and forces involved in the movement of oil drops. Mass and momentum equations are solved for single-phase flow and a Discrete Phase Model (DPM) is responsible for reproducing the dispersed phase behavior.

Assuming steady-state, incompressible, and turbulent flow, with an eddy viscosity-based model, the RANS (Reynolds-Averaged Navier-Stokes) continuity and momentum equations take the following form in the stationary reference frame, using the Einstein notation:

$$\frac{\partial U_i}{\partial x_i} = 0 \quad [4.7]$$

$$\rho \left( U_j \frac{\partial U_i}{\partial x_j} \right) = -\frac{\partial P}{\partial x_i} + \frac{\partial}{\partial x_j} \left( \mu_{ef} \left[ \frac{\partial U_i}{\partial x_j} + \frac{\partial U_j}{\partial x_i} \right] \right) \quad [4.8]$$

The water velocity,  $U$ , is evaluated at an inertial frame. The variable  $t$  indicates the time and  $x$  represents the position. Water density,  $\rho$ , and effective viscosity,  $\mu_{ef}$ , characterize the continuous phase. The modified pressure,  $P$ , is defined as  $P = p + \frac{2}{3}\rho\kappa\delta_{ij}$ , where  $p$  symbolizes the static pressure and  $\kappa$  the turbulent kinetic energy.

## 5. Numerical Methodology

Based on the original Baker-Hughes P23 ESP, two computational models were designed for the visualization prototype: the Full Geometry (FG), which reproduces with fidelity the real pump-based prototype, and the Reduced Geometry (RG), which is used for the mesh sensitivity analysis with much lower computational costs.

Both geometries, shown in **Fig. 7**, are composed of two main parts: the impeller zone, which has a rotational movement, reproduced by a Moving Reference Frame (MRF), and a stationary zone, corresponding to the diffuser. Although a Sliding Mesh Model (SMM) could provide higher fidelity results by taking into account the transient effects, the Moving Reference Frame (MRF) approach was found to provide acceptable results for the present purposes at a much lower computational cost. The realizable  $\kappa$ - $\epsilon$  turbulence model was chosen with a scalable wall function, which assured that results were consistent even in the case of a dimensionless distance from the wall of  $y^+ < 11$ . The model solves for two additional transport equations to determine the turbulent kinetic energy ( $\kappa$ ) and its dissipation ( $\epsilon$ ), which are needed for calculating the effective viscosity,  $\mu_{ef}$ . Further details about the model formulation may be taken from ANSYS Inc (2015).

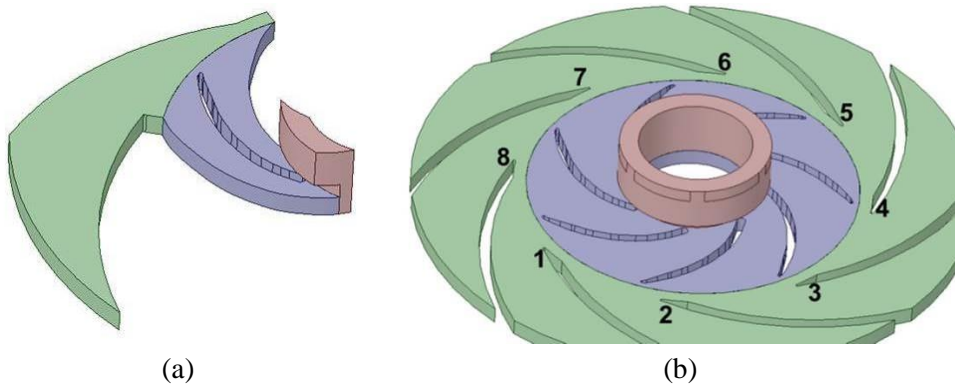


**Fig. 7.** Computational models for the ESP: (a) Reduced Geometry (RG) and (b) Full Geometry (FG).

Six simulations were prepared and performed, in accordance with the test matrix presented in **Table 1**. All cases were simulated in ANSYS<sup>®</sup> Fluent v16 software. The inlet condition was set as Mass Flow Average and adjusted according to each case. The outlet was set to Pressure-Outlet with gauge pressure 0 Pa. The SIMPLE scheme was used for pressure-velocity coupling and a second-order upwind scheme was chosen for spatial discretization. Convergence was attained when all residuals were below  $10^{-4}$ .

Once the flow solution had been obtained, a Lagrangian particle tracking was performed in the fixed velocity field; the one-way coupling is justifiable on the basis of the very low volume fraction of the disperse phase. A mono-dispersed distribution of oil drops was injected at the inlet surface with the same velocity magnitude as that of water; Equation [4.1] was integrated numerically to obtain the position as a function of time of tracking. The particles were tracked at a maximum of 5000 steps, sufficient for at least 90% of oil drops to leave the system. The drops are assumed to maintain a constant diameter (10 mm, 1 mm, 0.1 mm or 0.01 mm) in the complete duration of the simulation, without breaking up, which is consistent with experimental observations.

An automated routine was implemented to acquire and process data relative to the particle ID, position, velocity, turbulent eddy dissipation and drag and pressure forces.

## 6. Results

The experimental procedure provided quantitative results with respect to the pump performance and the oil drop dynamics. Similarly, the numerical approach also produced results concerning the prototype performance and the oil drop motion. Position, trajectory, turbulent dissipation, residence time, velocities, accelerations and forces are presented and compared in the next sections.

### 6.1 Mesh Sensitivity

The prototype geometry is originally not axisymmetric, due to differences between the number of impeller and diffuser blades. In the RG model, the diffuser regions were modified to present the same number of blades as the impeller, i.e., 7 instead of 8 blades, rendering the ESP an axisymmetric geometry. This was carried out

to ensure an efficient mesh-sensitivity analysis, in terms of computational costs, which is important for verifying the mesh independence of results. Four meshes were generated, following the characteristics displayed in **Fig. 8**. The mesh sensitivity analysis was performed for a rotation  $N = 3500 \text{ rpm}$  at a flow rate  $Q = 15.0 \text{ m}^3/\text{h}$ , a BEP condition.

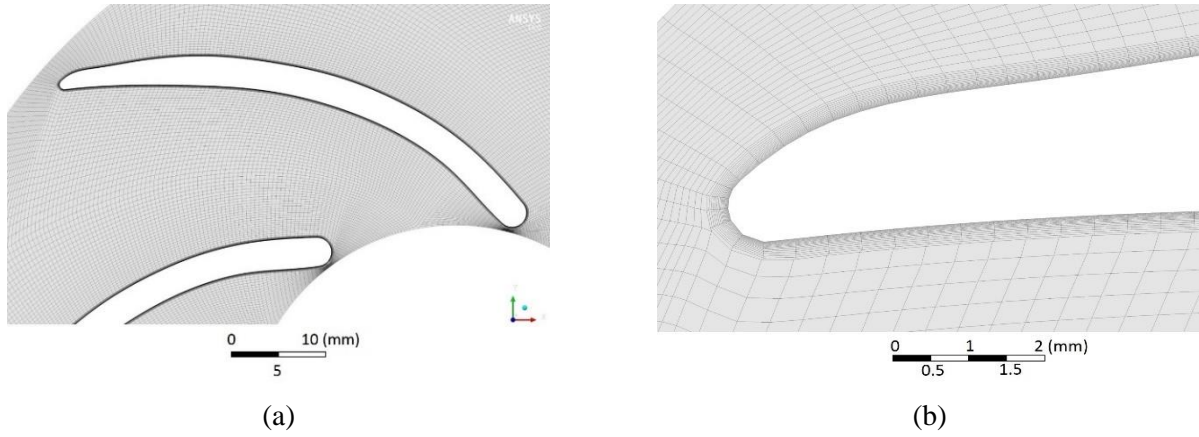


**Fig. 8.** Mesh grid of (a) impeller zone and (b) details of prisms layers near the blades.

The result is presented in **Fig. 9**, which shows the pump head convergence plotted as a function of the number of cells. The solution becomes independent when the number of cells is approximately 530k and the pump head relative error is less than 3%, using as reference the solution obtained for a mesh with 890k cells. Compared with experimental data (Biazussi, 2014), the pump head variation is  $\sim 12\%$ . This mesh presents an average dimensionless distance from the wall of  $y^+ \sim 10$ ; as mentioned in section 5, this is acceptable for the chosen wall function formulation.

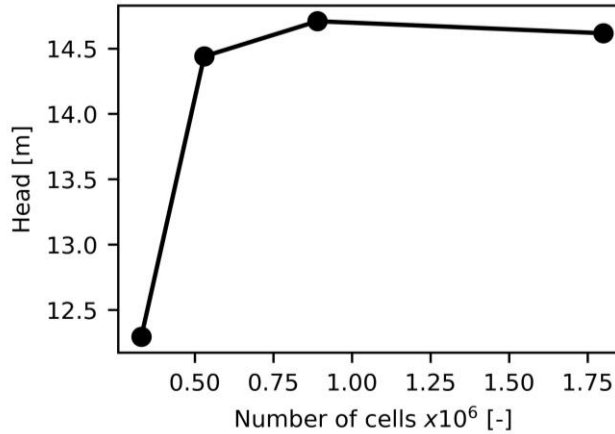


**Fig. 9.** Influence of grid size on simulated ESP head.

## 6.2 Pump Performance

Numerical and experimental results for single-phase pump performance curves were obtained using the dimensionless flow rate ( $\Phi$ ) and head ( $\Psi$ ) coefficient definitions:

$$\Phi = \frac{Q}{\omega D^3} \quad [6.1]$$

$$\Psi = \frac{\Delta P}{\rho \omega^2 D^2} \quad [6.2]$$



where  $Q$  represents the water flow rate,  $\Delta P$  symbolizes the difference between the outlet and inlet pressures,  $\omega$  designates the impeller angular speed and  $D$  corresponds to the impeller diameter.

Curves for the dimensionless head ( $\Psi$ ), as a function of the dimensionless flow rate ( $\Phi$ ), are exposed in **Fig. 10**. The results were obtained from experimental measurements and calculations via numerical simulations. As can be observed, CFD points and experimental curves present a satisfactory agreement, which indicates that the methodology adopted to carry out the simulations can predict very well the real flow inside the prototype pump.

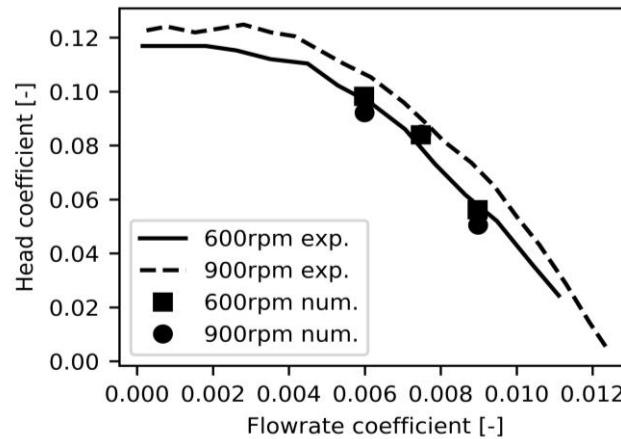


**Fig. 10.** Experimental and numerical performance of the ESP prototype operating with a single-phase flow.

The experimental head curves of the prototype operating with the oil-in-water dispersion suggest that the oil injection does not significantly modify the ESP performance. For the operational conditions investigated in this study, the curves of two-phase oil-water flow showed excellent agreement with the curves of single-phase water flow, with deviations less than 2% in the pressure increment. This difference is smaller than the experimental uncertainties. For larger oil fractions, evidently, instabilities, phase inversion, and performance degradation are expected. However, in this research, the results indicate that the addition of 2 ml/s of oil does not cause performance losses to the prototype. Indeed, the oil flow rate is less than 1% when compared to the water flow rates at the best efficiency points.

Monte Verde *et al.* (2017) also executed single-phase flow experiments and concluded that the performance curves for the visualization prototype are quite similar to the curves for the original Baker-Hughes P23 ESP. Hence, the modifications applied to the ESP to obtain the prototype for flow visualization did not significantly influence the pump characteristics, so the dynamic similarity was maintained and the flow fields in the impeller are fully representative.

### 6.3 Flow Field

Detailed insight into the flow field within the pump may be obtained through CFD simulations. Velocity contour was plotted in a plane parallel to the visualization area,  $z = -3$  mm, i.e., situated three millimeters below the top window. This plane contains the impeller zone and the diffuser zone. Results are presented in **Fig. 11** for the rotation speed  $N = 600$  rpm. According to Monte Verde *et al.* (2017), the blade height, which corresponds to the distance between the transparent top window and the white impeller bottom, is 6 mm.

As can be seen, **Fig. 11** presents the velocity contours in an inertial frame, for 600 rpm, at the BEP. For this condition, the jets formed at the diffuser region are slightly asymmetric and are located mostly under the diffuser blade. High-speed areas are seen at the impeller tips. The result suggests that the impeller-discharged oil drops that follow through the suction diffuser region could experience greater acceleration than other oil drops.

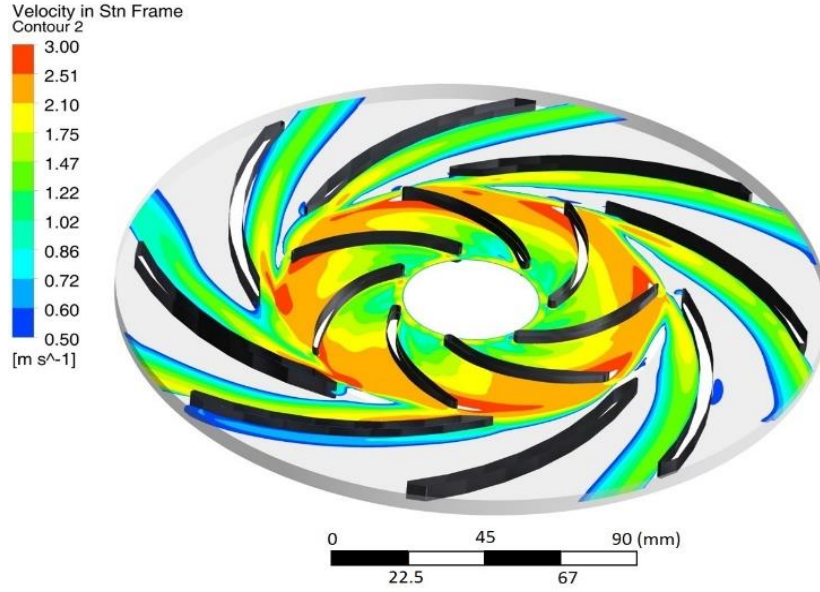


**Fig. 11.** Velocity contour curves at a  $xy$  plane ( $z = -3$  mm) for 600 rpm simulation at  $1.0 Q_{BEP}$ .

Motivated by the importance of models that describe the drop breakage events, a second analysis was conducted: the evaluation of the flow rate effect on the turbulent energy dissipation rate ( $\epsilon$ ), normalized by  $N^3 D^2$ , for both rotational speeds of 600 rpm and 900 rpm. Results can be found in **Fig. 12**, which introduces the volumetric average of the dimensionless turbulent energy dissipation rate for the impeller and diffuser regions, as a function of the flow rate. It can be observed that the 600 rpm and 900 rpm curves for each region collapse, a fact that suggests the normalization is appropriate and  $\epsilon \sim N^3 D^2$  indeed.

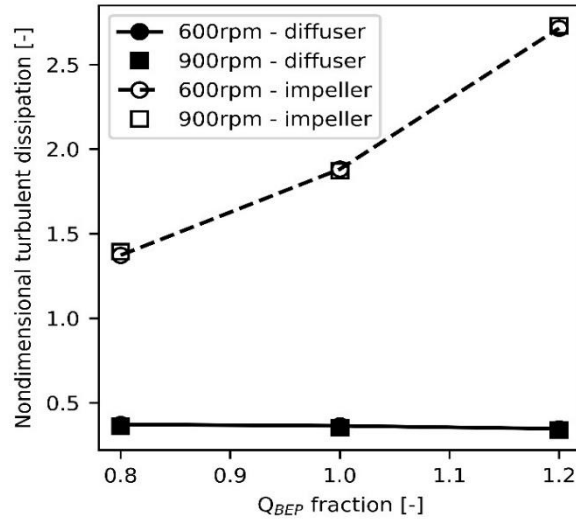


**Fig. 12.** Dimensionless turbulent energy dissipation rate calculated as a function of the flow rate.

The regions clearly present distinct behavior. The energy dissipated in the impeller region is influenced by the flow rate. A good fit for the dependence is described below, where  $q$  is the fraction of  $Q_{BEP}$ :

$$\frac{\epsilon}{N^3 D^2} = 0.3567 e^{1.6822 q} \quad [6.3]$$

On the other hand, the energy dissipation in the diffuser region is nearly constant, independent of the flow rate. The results can be explained by observing the contours of the normalized turbulent eddy dissipation.

Qualitative comparisons of this field are exposed in **Fig. 13**: (a-b) for different rotation speeds, at a constant  $1.0 Q_{BEP}$  condition, and (c-d) for various flow rates, at a constant impeller rotational speed  $N = 600 \text{ rpm}$ .

In **Fig. 13(a-b)**, flows are similar for both rotational speeds analyzed, which means not only the average of energy dissipation but also the field itself scales as  $\epsilon \sim N^3 D^2$ . However, in **Fig. 13(c-d)**, the high dissipation zone, located near the impeller blades, tends to expand with the flow rate rise, especially close to the leading edge. It explains the exponential increase in the curve presented in **Fig. 12**.

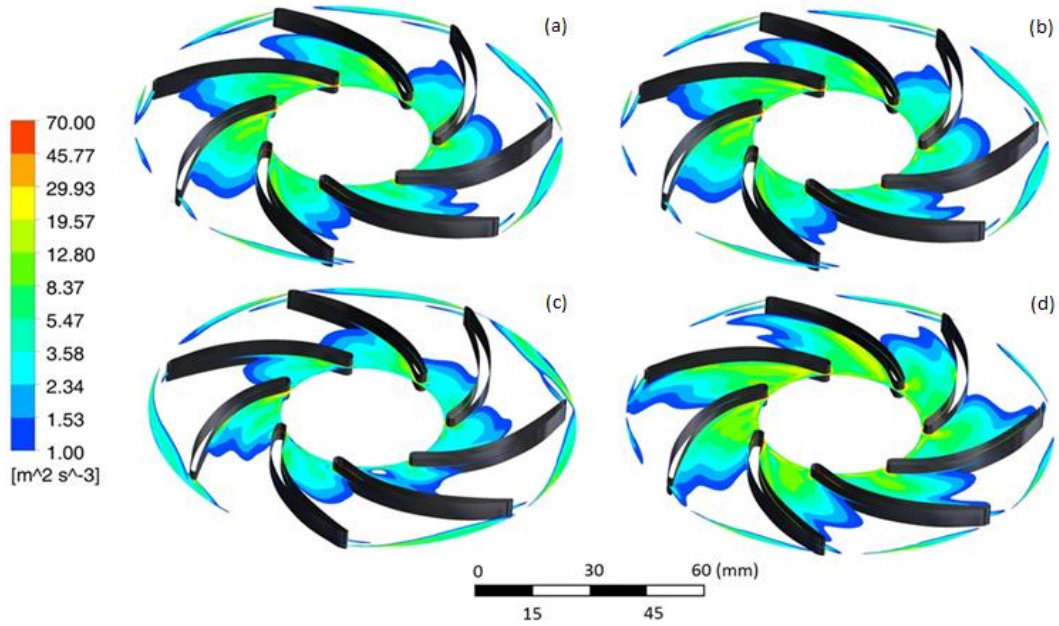


**Fig. 13.** Contour of normalized turbulent dissipation: at  $1.0 Q_{BEP}$  condition (a) for 600 rpm and (b) 900 rpm; fixing the impeller rotational speed at 600 rpm (c) for  $0.8 Q_{BEP}$  and (d)  $1.2 Q_{BEP}$ .

It is expected that the oil drops crossing zones of high dissipation, indicated in **Fig. 13**, are exposed to intense turbulence, which may result in a higher probability of breakage events and consequently smaller drop sizes. Notwithstanding, experimental observations (section 3.1) suggest the occurrence of breakage events mostly before the impeller zone. This is better illustrated in **Fig. 14**, which presents the contour of normalized turbulent energy dissipation rates plotted on an axial plane,  $y = 0$ .

As **Fig. 14** reveals, the prototype geometry has a contraction followed by a flow direction change of  $90^\circ$  at the impeller zone entrance. In this region, high turbulent energy dissipation rates are observed. Therefore, there are two main zones of high-intensity turbulence: in the impeller zone entrance (the most significant) and inside the impeller channels. The result corroborates with the experimental observations and implies that, in the present cases, the oil drop breaks up before entering the impeller channel.

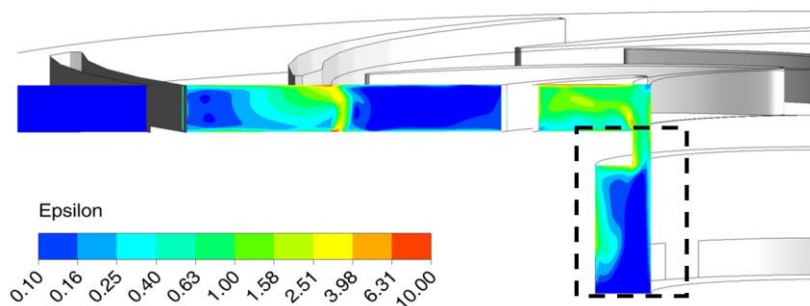


**Fig. 14.** Contour of normalized turbulent dissipation at an axial plane ( $y = 0$ ) and turbulent eddy dissipation  $\epsilon$  calculated from oil drop trajectories.

### 6.4 Drop Trajectory

An analysis of the processed images revealed that, in general, most oil drops followed random trajectories in the channels. Many drops underwent lateral deviations in their paths, while others moved in a parallel fashion to the blades. Some drops remained close to a blade, while others moved away from it.

Despite the randomness, three trajectory patterns were easily identified. And an oil drop can be classified into three categories, according to its trajectory: (a) oil drop with a central path, (b) oil drop near a suction blade, and (c) oil drop near a pressure blade.

Only a few drops follow the suction or pressure paths. Usually, these patterns occur when an oil drop is very close to the blade, almost sliding over it. In this situation, the particle-wall interaction is stronger than the particle-fluid interaction. As a result, the turbulent flow, full of vortices, jets and recirculation, cannot influence the oil drop trajectory.

On the other hand, many drops present the central path pattern. They enter the impeller next to the suction blade but gradually deviate towards the pressure blade, where they finish the trajectory and exit the impeller. The result is an approximately curved diagonal track. The central-path drops perform a quite long trajectory, since they cross the channel with the largest radial and transverse displacements.

The oil drop trajectories are illustrated in **Fig. 15**: (a-c) with the experimental paths observed in the processed flow images, and (d-f) showing the numerical reproduction of an oil-tracking experiment. The results embrace simulations at  $N = 600 \text{ rpm}$  and  $1.0 Q_{BEP}$  condition for oil drops with a diameter  $d = 1 \text{ mm}$ .

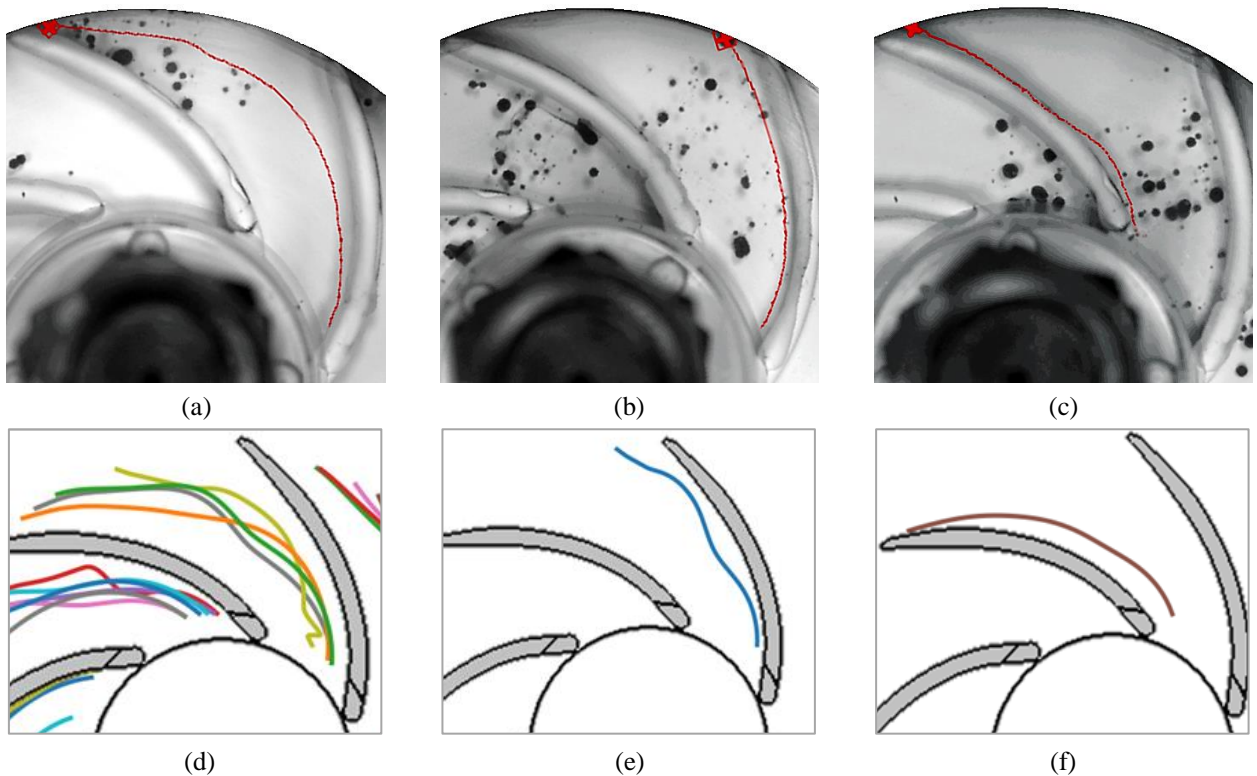


**Fig. 15.** Experimental observation of three patterns for an oil drop path: (a) central, (b) on suction blade, (c) on pressure blade; and numerical reproduction of paths: (d) central, (e) on suction blade, (f) on pressure blade.

In order to allow a systematic comparison between experimental and numerical results, the characteristic paths were translated to a set of empirical mathematical criteria. First, the oil drops' polar position inside the impeller,  $R$  and  $\theta$ , was normalized according to new radial and transverse terms,  $R^*$  and  $\theta^*$ , by the following definitions:

$$R^* = \frac{R - R_i}{R_o - R_i} \quad [6.4]$$

$$\theta^* = \frac{\theta + A \ln\left(\frac{R}{R_o}\right) + \theta_0}{\theta_c} \quad [6.5]$$

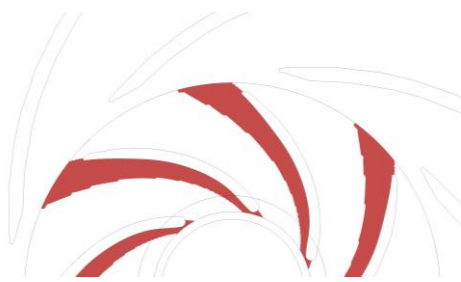


where  $R_i$  and  $R_o$  are the impeller radius from the origin to the inlet and to the outlet respectively, that is  $R_i = 0.027 \text{ m}$  and  $R_o = 0.056 \text{ m}$ , according to Monte Verde *et al.* (2017);  $A = -1.35$  is a constant that depends on the blade geometry;  $\theta_0$  is the drop's initial angle in relation to the  $x$  axis, a parameter dependent on the impeller position;  $\theta_c$  is the channel angle, given by:

$$\theta_c = \frac{2\pi}{N_c} \quad [6.6]$$

where  $N_c = 7$  represents the number of channels.

Then, with  $R^*$  and  $\theta^*$  values, three regions can be defined as described in **Table 2**, formulated to encompass the experimental classification itself.  $\theta^* < 0.4$  characterizes the suction zone. In case of  $\theta^* > 0.6$ , the zone is classified as pressure. Finally, the central path is described from two position functions,  $f^+(R^*)$  and  $f^-(R^*)$ .

**Table 2.** Oil drop paths: description of criteria and regions.

Criteria	Regions
Suction blade region	
$\theta^* < 0.4$	
Pressure blade region	
$\theta^* > 0.6$	
Central path	
$(\theta^* < f^+(R^*)) \wedge (\theta^* > f^-(R^*))$ $f^-(R^*) = 0.5R^*$ $f^+(R^*) = 0.5R^* + 0.5$	



A trajectory is classified as belonging to a determined path if the oil drop crosses the entire impeller zone without leaving its defined region. As already explained, the image observation from the experiments revealed that most oil drops presented random trajectories, preventing them from being classified into any of the regions.

From 103 particles injected in the numerical simulations, at least 30% passed through the classified regions and could be accounted for. Therefore, the numerical procedures resulted in a satisfactory qualitative agreement with the experimental visualizations.

### 6.5 Drop Dynamics

This section discusses the experimental and numerical results concerning velocities, accelerations, and forces related to the oil drop motion.

A numerical analysis of velocity profiles along the oil drop trajectories at the central region was conducted and compared to the experimental calculations. The average of radial and swirl velocities for 44 oil drops were calculated at 600 rpm and  $1.0 Q_{BEP}$  condition. Results are presented in **Fig. 16**. The average values are plotted along with bands representing a 95% confidence interval.

Radial and swirl accelerations were also calculated at 600 rpm and  $1.0 Q_{BEP}$  condition and the results are shown in **Fig. 17**. 31 oil drops with a constant diameter  $d = 1 \text{ mm}$  were analyzed. The acceleration plots also present the profiles obtained through a simulation that neglects the virtual mass term (VM). For the sake of clarity, dispersion bands were not drawn in the figures. Both analyses were performed using the non-inertial reference frame.

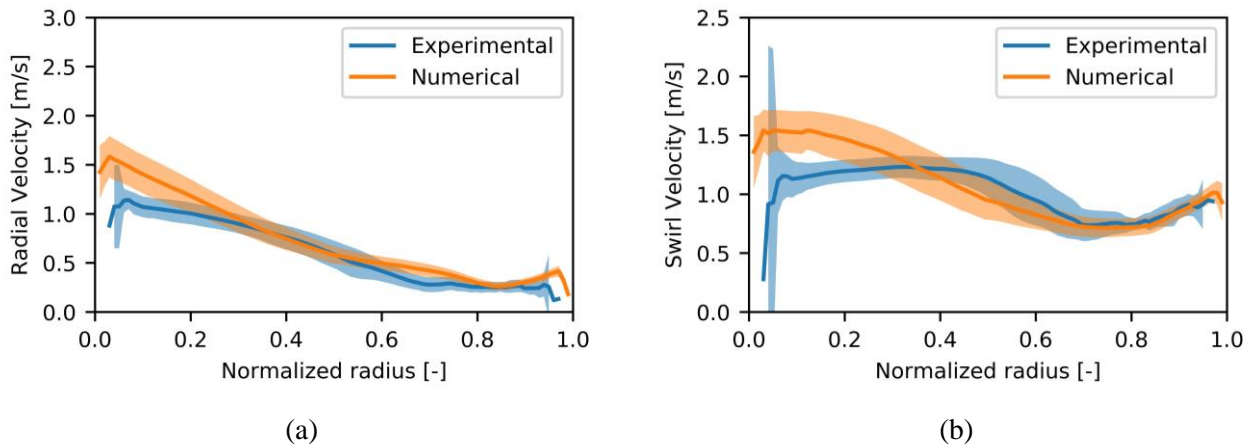


**Fig. 16.** Average velocity components at 600 rpm and  $1.0 Q_{BEP}$  condition for 44 drops with  $d = 1 \text{ mm}$ : (a) radial velocity and (b) swirl velocity.

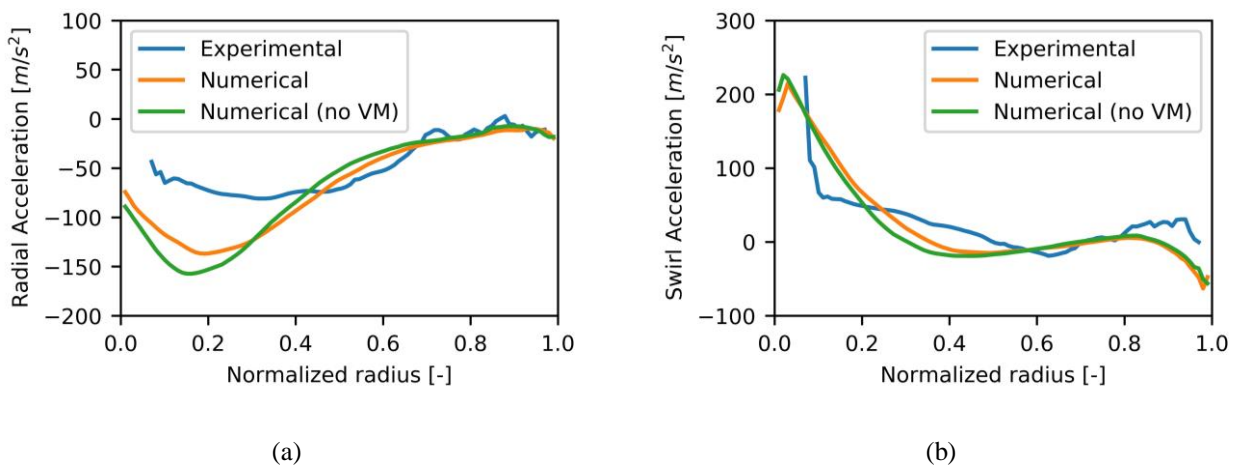


**Fig. 17.** Average acceleration components at 600 rpm and  $1.0 Q_{BEP}$  condition for 31 drops with  $d = 1 \text{ mm}$ : (a) radial acceleration and (b) swirl acceleration.



The oil drops' velocity components have magnitudes of up to 2.0 m/s, while the acceleration components take very high values, on the order of hundreds of  $\text{m/s}^2$ , from -150 to 200  $\text{m/s}^2$ . Both experimental and numerical results are directly dependent on the flow conditions. Moreover, both velocity and acceleration magnitudes present their peak values around the inner radius. The effect of virtual mass is small and most relevant in the entry region for the radial component of acceleration.

In general, the numerical and experimental results present satisfactory agreement for all cases. Deviations are expected due to the use of the MRF approach, which is not capable of capturing inherent unsteadiness. As a frozen-impeller approach, the MRF may give acceptable approximations when the interaction between moving and stationary parts is not strong and the flow at the interface between rotating and fixed regions does not present complicated features. Furthermore, it may be an interesting tool with which to evaluate the influence of different parameters on the overall flow behavior, as performed here (e.g., effect of flow rate and rotational speed on different variables). Differences between the experimental and numerical results may also be attributed to the assumption of a mono-dispersed distribution. In reality, there is a poly-dispersed distribution of drops and the interaction forces depend on the drop size, which in turn affect the trajectories. These effects can be especially important when strong accelerations are present, such as in the impeller inlet region, where larger deviations are seen in **Fig. 16**.

As noted in the section 4, the forces acting on the oil drops are due to drag, pressure gradient, and virtual mass. Vectors of pressure gradient were plotted in a plane parallel to the visualization area,  $z = -3 \text{ mm}$ , three millimeters below the top window. The results are presented in **Fig. 18**. Also mentioned before is the fact that the pressure force acting on the drop is proportional to the pressure gradient, in the opposite direction.

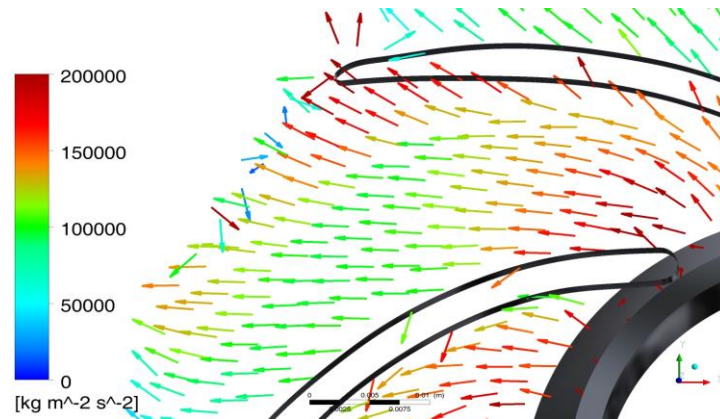


**Fig. 18.** Vectors of pressure gradient plotted on  $xy$  plane ( $z = -3 \text{ mm}$ ) for 600 rpm at 1.0  $Q_{BEP}$  condition.

The vectors in **Fig. 18** allow an assessment of the effect of the pressure gradient force on the drop trajectories in the impeller channel. When an oil drop moves near the suction region, it comes across a high adverse pressure gradient that causes it to divert its trajectory toward the central region. On the other hand, when an oil drop moves near the pressure blade, it also suffers influence from an adverse pressure gradient and tends to deviate in the direction of the pressure blade wall. The results explain why the oil drops preferably perform trajectories in the central region rather than close to the blades.

Shown in **Fig. 19** is a comparison between the magnitudes of drag and pressure forces, along with the resulting acceleration in the inertial frame. The analysis is restricted to the central region of the impeller, with the normalized radius,  $R^*$ , ranging from 0.3 to 0.7. In the present case, the pressure force is the most important force acting on the oil drop, being about 10 times larger than the drag effects. Yet, in the impeller entry region, other forces, such as drag and virtual mass, may contribute towards decelerating the oil drop. It is important to note, however, that these effects scale differently with drop size, such that this trend may be reversed in the case of fine dispersions.

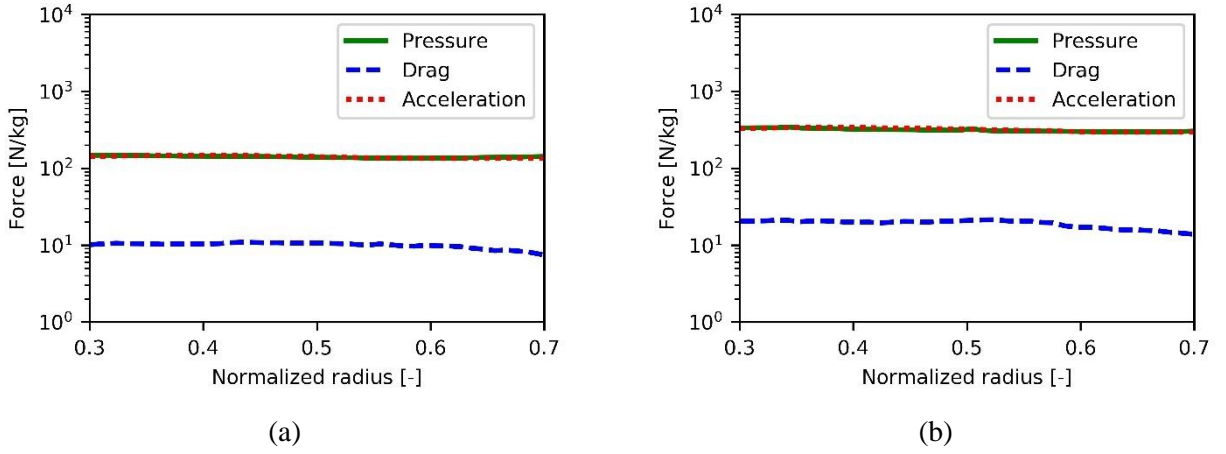


**Fig. 19.** Average drag force, pressure force, and acceleration in inertial frame for oil drop with  $d = 1 \text{ mm}$ : (a) central region at 600 rpm and (b) central region at 900 rpm.

Results for the oil drop tracking at 600 rpm and 900 rpm for 1.0  $Q_{BEP}$  conditions were compared using two global parameters: the normalized impeller residence time,  $t_{res}^*$ , and the particle Reynolds number,  $Re_d$ , both defined as follows:

$$t_{res}^* = t_{res} \frac{Q}{D^3} \quad [6.7]$$

$$Re_d = \frac{\rho_o d U_{tip}}{\mu} \quad [6.8]$$

where  $t_{res}$  is the impeller residence time, defined as the time spent by an oil drop moving from the inlet to the outlet of the impeller zone;  $Re_d$  is based on the blade velocity,  $U_{tip}$ , and also depends on the water viscosity,  $\mu$ ; As mentioned before,  $Q$  represents the water flow rate,  $D$  describes the impeller diameter,  $\rho_o$  corresponds to the oil density, and  $d$  symbolizes the drop diameter.

Results for  $t_{res}^*$  as a function of  $Re_d$  are shown in **Fig. 20** for all the conditions displayed in **Table 1**. Oil drops with  $d = 0.01 \text{ mm}$  and  $d = 0.1 \text{ mm}$ , corresponding to  $Re_d = 29.768$  and  $Re_d = 297.68$ , have similar normalized residence time for all cases. This observation may be expected since small oil drops tend to follow the water streamlines. As the oil drop sizes increase, the residence time at the impeller zone also increases.

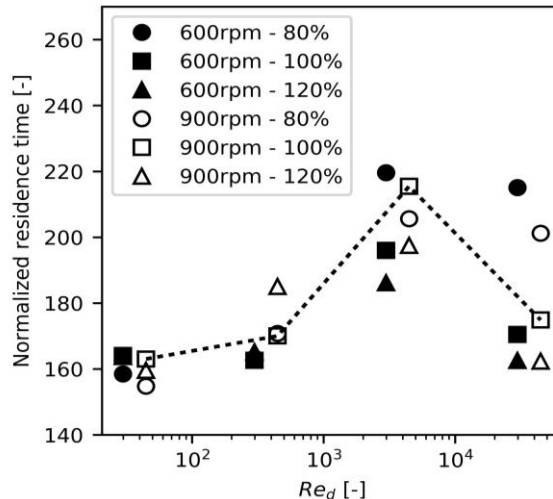


**Fig. 20.** Normalized impeller residence time  $t_{res}^*$  as function of  $Re_d$  for 600 rpm and 900 rpm.

Surprisingly, oil drops with  $d = 1 \text{ mm}$  ( $Re_d = 2976.8$ ) demonstrated higher residence times than oil drops with  $d = 10 \text{ mm}$  ( $Re_d = 29768$ ), except for in the  $0.8 Q_{BEP}$  condition. This can be explained by the observation that there is a significant decrease in the number of drops with  $d = 10 \text{ mm}$  captured at the central region, as **Table 3** shows. As this is the longest path out of the three categories, a lower number of drops leads to a reduced residence time. For the  $0.8 Q_{BEP}$  case, however, at both impeller rotation speeds, this effect seems to be balanced out by the presence of recirculation zones, which cause some oil drops to deviate and their residence time to be increased.

**Table 3.** Number of oil drops with different diameters captured in the central region.

$N$ [rpm]	$d$ [mm]	Number of drops		
		$0.8 Q_{BEP}$	$1.0 Q_{BEP}$	$1.2 Q_{BEP}$
600	0.01	27	33	35
	0.1	32	27	36
	1	34	36	34
	10	15	20	22
900	0.01	23	32	37
	0.1	28	27	37
	1	21	31	22
	10	15	19	20

The residence time reflects the time that the oil drops are exposed to breakage and coalescence events, so it is relevant to understand the dynamics of the oil motion. In addition, this knowledge can be important for scaling up pump operations.

To help illustrate how the different forces may impact the oil drop motion, **Fig. 21** presents a water streamline and trajectories of oil drops of various sizes. The injection was performed through a single point. Confirming previous results, small oil drops tend to follow the streamline. On the other hand, oil drops with  $d > 0.1 \text{ mm}$  show a deviation away from the same streamline. This fact suggests that oil drops with typical sizes as the ones measured in the present experiments are significantly influenced by external forces.

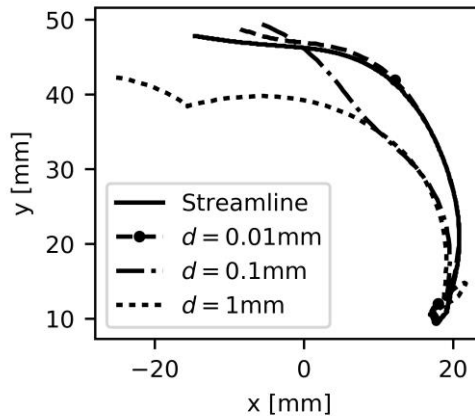


**Fig. 21.** Water streamline and single drop trajectories at 600 rpm

## 7. Conclusions

This work carried out experimental and numerical analyses on the motion of individual oil drops in a water flow within an ESP impeller.

Experimental tests were performed using a facility with an ESP prototype, the transparent top shroud of which enabled visualization of the flow in all the channels. The images revealed, in all operational conditions, a unique flow pattern within the impeller, a dispersion of oil drops in a continuous water phase. Most oil drops presented spherical geometry and only a few had irregular shapes. Almost no breakage and coalescence were observed within the channels. The oil drop diameter varied from approximately tenths of a millimeter to 3 mm. The images suggested a dependence between the oil drop size and the operational conditions. As the impeller rotation speed and the water flow rate increased, the oil drops became smaller.

Oil drops that follow central trajectories in the channels were investigated with respect to the dynamics of their motion. This motion is mainly governed by phenomena classified as particle-fluid interaction, in which three forces are in play: drag force, pressure gradient force, and virtual mass force. Flow images were processed for velocity, acceleration, and force calculation. The oil drops presented velocities with a magnitude of units of m/s, while accelerations reached hundreds of  $\text{m/s}^2$ . To verify the methodology, the measured pump performance was compared with previous single-phase experiments. The comparison revealed that the oil flow rate had very little effect on the pressure gain.

A numerical procedure was also adopted to determine the drop dynamics. The drop trajectory classes were defined in terms of normalized coordinates inside the impeller, which allowed for a systematic comparison between the results. The qualitative behavior of the paths was shown to be well reproduced by the adopted methodology. Comparisons of predicted and measured velocity and acceleration components along the radial position were made, deeming the agreement acceptable, given the limitations in the modeling.

An evaluation of the main forces involved in the oil drop motion indicated that the dominant force was that of pressure gradient, and its numerical values were about one order of magnitude larger than those of drag force. Virtual mass forces were observed to have some influence only at the impeller entrance. Finally, the evaluation of global parameters, such as impeller residence time, single oil drop trajectories, and static pressure provided an overview of how external forces act on oil drops. Small drops follow the water streamlines while oil drops with large diameters are affected by external forces in different ways and deviate from the continuous phase motion. In general, the oil drops suffer the influence of an adverse pressure gradient and tend to deviate from the suction blade to the pressure blade, a situation that facilitates the occurrence of central trajectories.

This study aims to open the way for greater phenomenological understanding and should be able to facilitate the creation of simplified models that may help the design and operation of ESP devices in challenging conditions. Such a framework could enable, for example, a parametric analysis of operating conditions, as well as a coupling to one-dimensional multiphase flow models.

## Acknowledgements

The authors would like to thank Statoil Brazil, ANP (“Compromisso de Investimentos com Pesquisa e Desenvolvimento”) and PRH/ANP for providing financial support for this work. The acknowledgements are also extended to Center for Petroleum Studies (CEPETRO), University of Campinas (UNICAMP), Artificial Lift & Flow Assurance Research Group (ALFA), ISDB FlowTech and SINTEF-NO.

## References

- Abivin, P., Henaut, I., Chaudemanche, C., Argillier, J.F., Chinesta, F. “Dispersed systems in heavy crude oils”. *Oil & Gas Science and Technology*, Vol. 64, n. 5, p. 557-570, 2009. doi:10.2516/ogst/2008045
- Alkaya, B., Jayawardena, S.S., Brill, J.P. “Oil-water flow patterns in slightly inclined pipes”. *Energy for the New Millennium*, Vol. 14, n. 17, p. 1-8, 2000.

- Amaral, G., Estevam, V., Franca, F.A. "On the influence of viscosity on ESP performance", *SPE Productions & Operations*, Vol. 24, n. 2, p. 303-310, 2009. doi:10.2118/110661-PA
- Angeli, P., Hewitt, G.F. "Flow structure in horizontal oil-water flow". *International Journal of Multiphase Flow*, Vol. 26, n. 7, p. 1117-1140, 2000. doi:10.1016/S0301-9322(99)00081-6
- ANSYS Inc. "ANSYS Fluent Theory Guide", Release v16.2, 2015.
- Barrios, L., Prado, M.G. "Experimental visualization of two-phase flow inside an electrical submersible pump stage". *Journal of Energy Resources Technology*, Vol. 133, n. 4, 2011. doi:10.1115/1.4004966
- Barrios, L., Prado, M.G., Kenyery, F. "CFD modeling inside an electrical submersible pump in two-phase flow condition", *ASME 2009 Fluids Engineering Division Summer Meeting*, 2009.
- Biazussi, J.L., "A drift-flux model for gas-liquid flow in electrical submersible pump operating with low viscous liquid", PhD dissertation, University of Campinas, 2014.
- Brauner, N., Maron, D.M. "Flow pattern transitions in two-phase liquid-liquid flow in horizontal tubes". *International Journal of Multiphase Flow*, Vol. 18, n. 1, p.123-140, 1992. doi:10.1016/0301-9322(92)90010-E
- Bulgarelli, N.A.V., Biazussi, J.L, Castro, M.S., Monte Verde, W., Bannwart, A.C. "Experimental study of phase inversion phenomena in electrical submersible pumps under oil-water flow". *Proceedings of OMAE, the 36th International Conference on Ocean, Offshore & Arctic Engineering*. Trondheim, Norway, 2017a. doi: 10.1115/OMAE2017-61865
- Bulgarelli, N.A.V., Biazussi, J.L, Perles, C.E., Monte Verde, W., Castro, M.S., Bannwart, A.C. "Analysis of chord length distribution in phase inversion of water-oil emulsions at electrical submersible pump outlet". *Proceedings of ExHFT, the 9th World Conference on Experimental Heat Transfer, Fluid Mechanics and Thermodynamics*. Foz do Iguaçu, Brazil, 2017b.
- Caridad, J., Asuaje, M., Kenyery, F., Tremante, A., Aguillón, O. "Characterization of a centrifugal pump impeller under two-phase flow conditions". *Journal of Petroleum Science and Engineering*, Vol. 63, p. 18-22, 2008. doi:10.1016/j.petrol.2008.06.005
- Caridad, J., Kenyery, F. "CFD analysis of electric submersible pumps (ESP) handling two-phase mixtures", *Journal of Energy Resources Technology*, Vol. 126, p. 99-104, 2004. doi:10.1115/1.1725156.
- Castro, M.S., Pereira, C.C., Santos, J.N., Rodriguez, O.M.H. "Geometrical and kinematic properties of interfacial waves in stratified oil-water flow in inclined pipe". *Experimental Thermal and Fluid Science*, Vol. 37, p. 171-178, 2012. doi:10.1016/j.expthermflusci.2011.11.003
- Cavicchio, C.A.M., Biazussi, J.L, Castro, M.S., Bannwart, A.C., Rodriguez, O.M.H., Carvalho, C.H.M. "Experimental study of viscosity effects on heavy crude oil-water core-annular flow pattern". *Experimental Thermal and Fluid Science*, Vol. 92, p. 270-285, 2018. doi:10.1016/j.expthermflusci.2017.11.027
- Chang, C.H., Franses, E.I. "Adsorption dynamics of surfactants at the air/water interface: A critical review of mathematical models, data and mechanisms". *Colloids and Surfaces A: Physicochemical and Engineering Aspects*, Vol. 100, p. 1-45, 1995. doi:10.1016/0927-7757(94)03061-4
- Crowe, C., Sommerfeld, M., Tsuji, Y. "Multiphase Flows with Droplets and Particles". CRC Press, 1998.
- Cubas Cubas, J.M. "Experimental study of biphasic flow air-water in a radial centrifugal pump". Master's Thesis, Federal University of Technology, Paraná, Curitiba, Brazil, 2017.
- Estevam, V. "A phenomenological analysis about centrifugal pump in two-phase flow operation". PhD dissertation, University of Campinas, Sao Paulo, Brazil, 2002.
- Flatern, R.V. "The Defining Series - Electrical Submersible Pumps", *Oilfield Review*, 2015.
- Grassi, B., Strazza, D., Poesio, P. "Experimental validation of theoretical models in two-phase high-viscosity ratio liquid-liquid flows in horizontal and slightly inclined pipes". *International Journal of Multiphase Flow*, Vol. 34, n. 10, p. 950-965, 2008. doi:10.1016/j.ijmultiphaseflow.2008.03.006
- Hanafizadeh, P., Hojati, A, Karimi, A. "Experimental investigation of oil-water two phase flow regime in an inclined pipe". *Journal of Petroleum Science and Engineering*, Vol. 136, p. 12-22, 2015. doi:10.1016/j.petrol.2015.10.031
- Hibbeler, R.C. "Engineering Mechanics: Dynamics". 12th edition. Prentice Hall, 2010.
- Khalil, M., Kassab, S., Ismail, A., Elazab, I. "Centrifugal pump performance under stable and unstable oil-water emulsions flow". 12th International Water Technology Conference, Alexandria, Egypt, 2008.
- Loh, W.L., Premanadhan, V.K. "Experimental investigation of viscous oil-water flows in pipeline". *Journal of Petroleum Science and Engineering*, Vol. 147, p. 87-97, 2016. doi:10.1016/j.petrol.2016.05.010
- Lum, J.Y.L., Al-Wahaibi, T., Angeli, P. "Upward and downward inclination oil-water flows". *International Journal of Multiphase Flow*, Vol. 32, n. 4, p. 413-435, 2006. doi:10.1016/j.ijmultiphaseflow.2006.01.001

- Maindarkar, S.N., Hoogland, H., Henson, M.A. "Predicting the combined effects of oil and surfactant concentrations on the drop size distributions of homogenized emulsions". *Colloids and Surfaces A: Physicochemical and Engineering Aspects*, Vol. 467, p. 18-30, 2015. doi:10.1016/j.colsurfa.2014.11.032
- Minemura, K., Murakami, M. "A theoretical study on air bubble motion in a centrifugal pump impeller", *Journal of Fluids Engineering*, Vol. 102, p. 446-455, 1980.
- Mitre, J.F., Lage, P.L.C., Souza, M.A., Silva, E., Barca, L.F., Moraes, A.O.S., Fonseca, E.F. "Droplet breakage and coalescence models for the flow of water-in-oil emulsions through a valve-like element". *Chemical Engineering Research and Design*, Vol. 92, n. 11, p. 2493-2598, 2014. doi:10.1016/j.cherd.2014.03.020
- Mohammadi, M., Sharp, K.V. "Experimental techniques for bubble dynamics analysis in microchannels: a review". *Journal of Fluids Engineering*, Vol. 135, 2013. doi:10.1115/1.4023450
- Monte Verde, W., Biazussi, J.L., Sassim, N.A., Bannwart, A.C. "Experimental study of gas-liquid two-phase flow patterns within centrifugal pumps impellers". *Experimental Thermal and Fluid Science*, Vol. 85, p. 37-51, 2017. doi:10.1016/j.expthermflusci.2017.02.019
- Morales, R., Pereyra, E., Wang, S., Shoham, O. "Droplet formation through centrifugal pumps for oil-in-water dispersions", *SPE Journal*, Vol. 18, p. 172-178, 2013. doi:10.2118/163055-PA
- Morsi, S.A., Alexander, A.J. "An investigation of particle trajectories in two-phase flow systems". *Journal of Fluid Mechanics*, Vol. 55(2), p. 193-208, 1972.
- Mundo, D.D.C., "Study of oil/water flow and emulsion formation in electrical submersible pumps". Master's Thesis, The University of Tulsa, USA, 2014.
- Ofuchi, E.M., Ancajima, F.C., Stel, H., Neto, M.A.N., Morales, R.E.M. "Influence of operational conditions on the trajectory of an air bubble inside a centrifugal pump". *Proceedings of JEM, the IV Journeys in Multiphase Flow*. Sao Paulo, Brazil, 2017.
- Pineda, H., Biazussi, J.L., López, F., Oliveira, B., Carvalho, R. Bannwart, A.C., Ratkovich, N. "Phase distribution analysis in an Electrical Submersible Pump (ESP) inlet handling water-air two-phase flow using Computational Fluid Dynamics (CFD)". *Journal of Petroleum Science and Engineering*, Vol. 139, p. 49-61, 2016. doi:10.1016/j.petrol.2015.12.013
- Rodriguez, O.M.H., Baldani, L.S. "Prediction of pressure gradient and holdup in wavy stratified liquid-liquid inclined flow". *Journal of Petroleum Science and Engineering*, Vol. 96, p. 140-151, 2012. doi:10.1016/j.petrol.2012.09.007
- Rodriguez, O.M.H., Oliemans, R.V.A. "Experimental study on oil-water flow in horizontal and slightly inclined pipes". *International Journal of Multiphase Flow*, Vol. 32, n. 3, p. 323-343, 2006. doi:10.1016/j.ijmultiphaseflow.2005.11.001
- Sabino, R.H.G. "Analysis of dynamic of a gas bubble in a centrifugal pump" Master's Thesis, Federal University of Technology, Paraná, Curitiba, Brazil, 2015.
- Schilling, R., Frobenius, M. "Numerical simulation of the two-phase flow in centrifugal pump impellers", *ASME 2002 Fluids Engineering Division Summer Meeting*.
- Sjoblom, J. "Emulsions and Emulsion Stability: Surfactant Science Series". 2nd edition. CRC Press, 2005.
- Stel, H., Sirino, T., Ponce, F.J., Chiva, S., Morales, R.E.M. "Numerical investigation of the flow in a multistage electric submersible pump". *Journal of Petroleum Science and Engineering*, Vol. 136, p. 41-54, 2015. doi:10.1016/j.petrol.2015.10.038
- Takacs, G. "Electrical Submersible Pumps Manual". 2nd edition. Gulf Professional Publishing, 2017.
- Trevisan, F.E., Prado, M.G. "Experimental investigation of the viscous effect on two-phase flow patterns and hydraulic performance of electrical submersible pumps". *Journal of Canadian Petroleum Technology*, Vol. 50, p. 45-52, 2011. doi:10.2118/134089-PA
- Vielma, M., Atmaca S., Sarica, C., Zhang, H., "Characterization of oil/water flows in horizontal pipes", *SPE Annual Technical Conference and Exhibition*, Anaheim, California, USA, 2007.
- Wang, W., Gong, J., Angeli, P. "Investigation on heavy crude water two phase flow and related flow characteristics". *International Journal of Multiphase Flow*, Vol. 37, p. 1156-1164, 2011. doi:10.1016/j.ijmultiphaseflow.2011.05.011
- White, F.M. "Fluid Mechanics". 7th edition. McGraw-Hill, 2011.
- Zhang, J., Cai, S., Li, Y., Zhu, H., Zhang, Y. "Visualization study of gas-liquid two-phase flow patterns inside a three-stage rotodynamic multiphase pump". *Experimental Thermal and Fluid Science*, Vol. 70, p. 125-138, 2016. doi:10.1016/j.expthermflusci.2015.08.013
- Zhu, J., Banjar, H., Xia, Z., Zhang, H. "CFD simulation and experimental study of oil viscosity effect on multi-stage electrical submersible pump (ESP) performance". *Journal of Petroleum Science and Engineering*, Vol. 146, p. 735-745, 2016. doi:10.1016/j.petrol.2016.07.033